A priori analysis of differential diffusion for model development for scale-resolving simulations

Franziska Hunger,[1] Felix Dietzsch,[1,2] Michael Gauding,[3] and Christian Hasse[1,2]
[1]*Chair of Numerical Thermo-Fluid Dynamics, TU Bergakademie Freiberg, 09599 Freiberg, Germany*
[2]*Institute for Simulation of reactive Thermo-Fluid Systems, TU Darmstadt, 64287 Darmstadt, Germany*
[3]*CORIA, CNRS, UMR No. 6614, University of Rouen, 76801 Saint Etienne du Rouvray, France*

(Received 14 June 2017; published 8 January 2018)

The present study analyzes differential diffusion and the mechanisms responsible for it with regard to the turbulent/nonturbulent interface (TNTI) with special focus on model development for scale-resolving simulations. In order to analyze differences between resolved and subfilter phenomena, direct numerical simulation (DNS) data are compared with explicitly filtered data. The DNS database stems from a temporally evolving turbulent plane jet transporting two passive scalars with Schmidt numbers of unity and 0.25 presented by Hunger *et al.* [F. Hunger *et al.*, J. Fluid Mech. **802**, R5 (2016)]. The objective of this research is twofold: (i) to compare the position of the turbulent-nonturbulent interface between the original DNS data and the filtered data and (ii) to analyze differential diffusion and the impact of the TNTI with regard to scale resolution in the filtered DNS data. For the latter, differential diffusion quantities are studied, clearly showing the decrease of differential diffusion at the resolved scales with increasing filter width. A transport equation for the scalar differences is evaluated. Finally, the existence of large scalar gradients, gradient alignment, and the diffusive fluxes being the physical mechanisms responsible for the separation of the two scalars are compared between the resolved and subfilter scales.

DOI: 10.1103/PhysRevFluids.3.014601

I. INTRODUCTION

The mixing of two or more scalars is a process relevant to several engineering, environmental, and chemical applications. The separate evolution of initially perfectly correlated scalars in a turbulent or laminar flow caused only by different molecular diffusivities is termed differential diffusion. This phenomenon has been intensively investigated for decades. The first observation of differential diffusion was reported by Bilger [1] in a CH_4 diffusion flame. Experimental and numerical studies using reactive but also nonreactive flows followed. An overview on previous experimental and numerical investigations was given by Lavertu *et al.* [2]. Measurements of turbulent nonreacting liquid and gas-phase flows were performed to quantify differential diffusion (see, e.g., [3–5]). In addition, many nonreacting direct numerical simulations (DNSs) investigating differential diffusion in isotropic turbulence are reported in the literature (e.g., [6–8]). However, only few large-eddy simulations (LESs) of differential diffusion in nonreactive simulations have been performed, e.g., in [9,10]. Moreover, combustion can be strongly influenced by differential diffusion processes since it alters heat release rates due to altered species composition. Thus, reacting flows were also utilized to study the influence of turbulence on differential diffusion experimentally (e.g., [11–13]) and numerically using DNS (e.g., [14–16]) and LES (e.g., [17–19]). The general finding of both nonreacting and reacting investigations was an increase in differential diffusion with decreasing Reynolds number and increasing Schmidt number ratio. Further, the connection between small and large scales was analyzed and the presence of differential diffusion effects at large scales was confirmed, also allowing the detection of differential diffusion in very-well-resolved LESs.

Recent studies have discovered that the turbulent-nonturbulent interface (TNTI) is an important characteristic of the flow dynamics; a review is given by da Silva *et al.* [20]. The TNTI separates flow fields into turbulent and nonturbulent regions in free shear flows through vorticity and a sharp vorticity increase across the interface [21]. Experimental studies (e.g., [22–24]) and numerical studies (e.g., [21,25,26]) exist, applying different procedures to detect the interface position. These procedures are specifically the scalar-based criterion, which is often used in experimental studies due to the experimental accessibility of the scalar field and the vorticity criterion, which is often applied in DNS studies due to the high resolution of the flow field. The equivalence of the vorticity and scalar criterion for detecting the TNTI was shown by Gampert *et al.* [27] for a unity-Schmidt-number scalar. However, statistical differences exist when the Schmidt number is significantly lower [26]. Moreover, the general accessability of the TNTI detected with the scalar criterion in LESs was presented by Gampert *et al.* [28]. Due to high local gradients near the interface, molecular diffusion is expected to be important, which was confirmed by Watanabe *et al.* [21]. They showed that the molecular diffusion term in the scalar transport equation is important in the vicinity of the interface and that it significantly decreases towards the turbulent core region. This implies that differential diffusion is also important at the interface. A temporally evolving jet transporting two passive scalars with different Schmidt numbers was studied by Hunger *et al.* [26], focusing on differential diffusion. It was shown in this type of shear flow that differential diffusion mostly originates at the interface.

In summary, differential diffusion is a complex phenomenon. A number of studies have been conducted for reactive and nonreactive flows. However, no comprehensive theory exists describing all observed phenomena in the interplay of molecular differential diffusion and turbulence. Since differential diffusion is molecular in origin but propagates towards large scales, clear conclusions with respect to modeling and necessary scale resolution requirements in LESs to accurately describe differential diffusion are missing. The present study contributes to scale-resolved model development to incorporate differential diffusion in LESs. Therefore, the DNS data of a temporally evolving turbulent plane jet of two passive scalars with different Schmidt numbers [26] are explicitly filtered. First, the differences between the original DNS interface position and the interface detected on the filtered data are analyzed. Next, differential diffusion quantities are studied with regard to their existence at the resolved scales. A transport equation for the scalar differences is evaluated to quantify the resolution of the source term that generates differential diffusion. Finally, the existence of large scalar gradients, gradient alignment, and the diffusive fluxes are compared between the resolved and subfilter scales.

II. NUMERICAL APPROACH

A direct numerical simulation of a temporally evolving turbulent plane jet flow was carried out and described by Hunger *et al.* [26]. The DNS solves the nondimensional incompressible Navier-Stokes equations and transport equations for passive scalars. The convective term is formulated in skew-symmetric form to reduce aliasing errors. The spatial derivatives are treated by a sixth-order compact Padé scheme [29]. Temporal integration is performed by a low-storage, fourth-order Runge-Kutta scheme. The Poisson equation is solved in the spectral space by adapting a Helmholtz equation (see [30]).

The computational domain has periodic boundary conditions in the streamwise Ox and spanwise Oy directions and free-slip boundary conditions are used in the crosswise Oz direction. A scheme of the setup is shown in Fig. 1. The flow and the scalar fields are statistically homogeneous in the xOy planes. The nondimensional size of the domain is $L_x = 6\pi$, $L_y = 6\pi$, and $L_z = 12.5$, discretized by $2816 \times 2816 \times 1500$ grid points. A uniform mesh is used for the inner part of the domain, which is characterized by the homogeneous and equidistant grid width Δ_x, while the outer part is slightly coarsened towards the crosswise boundaries. The interfacial layer is resolved well with 14 grid points at the investigated instant, which is in the fully turbulent, self-similar regime (see Fig. 2). For the investigated instant ($t = 19$), the Taylor microscale-based Reynolds number Re_λ, the normalized jet thickness H, and the normalized center-plane value of the velocity $\langle U_c \rangle / U_0$ and of scalar 1,

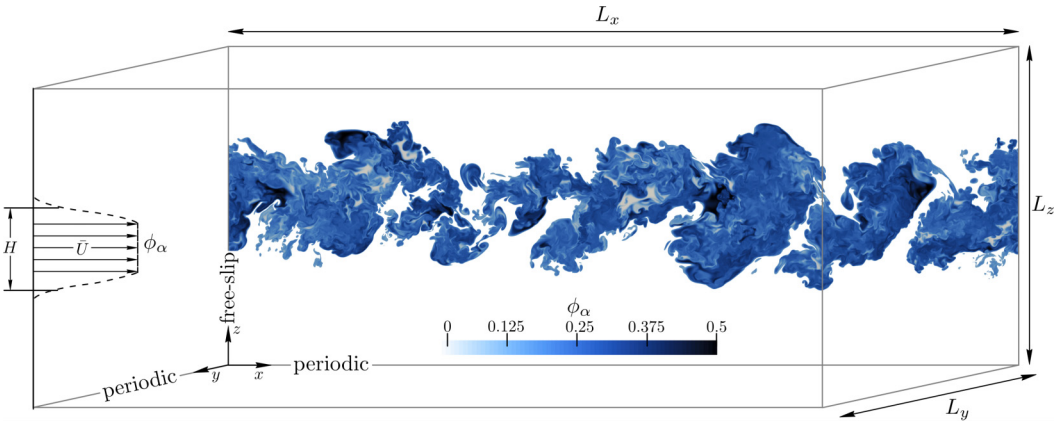

FIG. 1. Scheme of the DNS setup including the contour of the unity-Schmidt-number scalar in an xOz plane.

$\langle\phi_1\rangle_c/\phi_{1,0}$, are listed in Table I. Further at this instant, the Kolmogorov length scale η equals the grid width Δ_x. The transport equations are nondimensionalized by the initial maximum velocity $U_{\max,0}$, the initial jet thickness H_0, and the maximum value of the initial scalar profile $\phi_{\max,0}$. They read

$$\frac{\partial u_j}{\partial t} + u_i \frac{\partial u_j}{\partial x_i} = -\frac{\partial p}{\partial x_j} + \frac{1}{\mathrm{Re}_0} \frac{\partial^2 u_j}{\partial x_i \partial x_i}, \quad \frac{\partial u_i}{\partial x_i} = 0 \tag{1}$$

$$\frac{\partial \phi_\alpha}{\partial t} + u_i \frac{\partial \phi_\alpha}{\partial x_i} = \frac{1}{\mathrm{Pe}_{0,\alpha}} \frac{\partial^2 \phi_\alpha}{\partial x_i \partial x_i}, \quad \alpha = 1,2 \tag{2}$$

where α does not indicate index summation. The Péclet number is defined as $\mathrm{Pe}_{0,\alpha} = \mathrm{Sc}_\alpha \mathrm{Re}_0$, Re_0 denotes the initial jet Reynolds number equal to 8000, and the Schmidt number Sc_α is the ratio of kinematic viscosity ν and molecular diffusivity D_α set to 1 for ϕ_1 and to 0.25 for ϕ_2. Subsequently, all given quantities are normalized in the same way. The initial mean velocity profile is composed of two mirrored hyperbolic-tangent profiles with high stiffness. The mean half-width velocity profile is

$$\overline{U(z)}/U_0 = 1.0 + \tanh[(z + 0.5)/(2.0 \times 0.055)]. \tag{3}$$

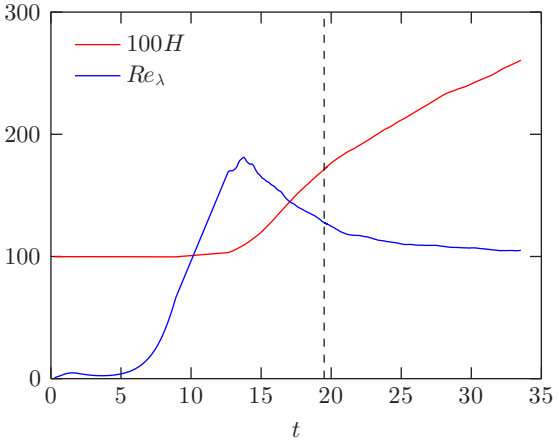

FIG. 2. Temporal evolution of the jet thickness H and the Taylor microscale-based Reynolds number at the jet center; the investigated time step ($t = 19$) is marked with a dashed line.

TABLE I. Flow properties at the investigated instant $t = 19$.

Property	Value
Re_λ	120
H	1.7
$\langle U_c \rangle / U_0$	0.59
$\langle \phi_1 \rangle_c / \phi_{1,0}$	0.48

Uncorrelated velocity fluctuations with an intensity of 5% are superimposed onto the mean profile around the shear layer and damped towards the center plane and the irrotational outer region. The two mean scalar profiles are initialized corresponding to the mean velocity profile, but nonperturbed.

A box filter in physical space was used for filtering the DNS data. This procedure has similarly been applied in *a priori* analyses for LES model development and evaluation, e.g., in [31–34]. Three different filter widths Δ were applied, namely, $\Delta = 7\Delta_x$, $\Delta = 15\Delta_x$, and $\Delta = 21\Delta_x$, and are used for comparing the influence of filtering on the evaluated quantities studied for detecting the TNTI and for analyzing differential diffusion. The corresponding mean profiles of the ratio of resolved turbulent kinetic energy $\overline{k}$ and total turbulent kinetic energy k in crosswise direction are shown in Fig. 3(a) and the one-dimensional spectra along the jet center plane are shown in Fig. 3(b). Further, the scalar spectra of the DNS data of both passive scalars are shown in Fig. 3(c) and the influence of the filtering procedure on the unity-Schmidt-number scalar is shown in Fig. 3(d). Note that with the filter size $\Delta = 7\Delta_x$, about 95% of the entire turbulent kinetic energy can be resolved. The filter size $\Delta = 15\Delta_x$ is well within the suggested resolution criterion of 80% [35]. The final filter width of $\Delta = 21\Delta_x$ drops below this criterion, but at least 75% of the turbulent kinetic energy can be resolved and thus this filter width can be considered reasonable for LES applications. The velocity spectra and the scalar spectra illustrate the nonlocality of the box filter in wave-number space, as described, e.g., in [35]. All statistics depend on the crosswise direction z. In the following, the statics are calculated by averaging over either the entire xOy plane or the surface with a constant distance from the TNTI.

III. RESULTS AND DISCUSSION

A. Detecting the turbulent-nonturbulent interface in filtered DNS data

Several criteria exist for detecting a TNTI (see, e.g., [20]). According to [26], the vorticity criterion and the scalar criterion are applied here, comparing their sensitivity to the filtering procedure.

Figure 4 shows an instantaneous distribution of the unity-Schmidt-number scalar ϕ_1 in a yOz plane comparing the original data taken from the left half of the plane with the filtered data taken from the right half of the plane, applying a filter width of $\Delta = 21\Delta_x$. Additionally marked are the corresponding vorticity interfaces of the original DNS and filtered data. Significant differences in the original and filtered scalar field are visible. However, the detected TNTI is qualitatively comparable. The detection of the interface using the scalar and the vorticity criterion is based on threshold values for both quantities. For the vorticity interface, parametric studies were performed similarly as shown by Bisset *et al.* [36]. The threshold values chosen are 2.5, 2, 1.1, and 1 for the DNS data and the filtered data of the present case, respectively, which show a continuous decrease with increasing filter width. The threshold value of the scalar defining the scalar interface position can be found using a probability density function (PDF) of the scalar at a crosswise position where the shape of the PDF is bimodal. This bimodal shape of the PDF can be found close to the TNTI making the minimum value of the PDF representative for the TNTI itself. The scalar threshold value then equals the value where the minimum of this PDF is found (see [37]). These PDFs are presented in Fig. 5 for the unity-Schmidt-number scalar, where only the range of $\phi_1 = [0,0.2]$ is shown in order to visualize the small but continuous decrease of the threshold values.

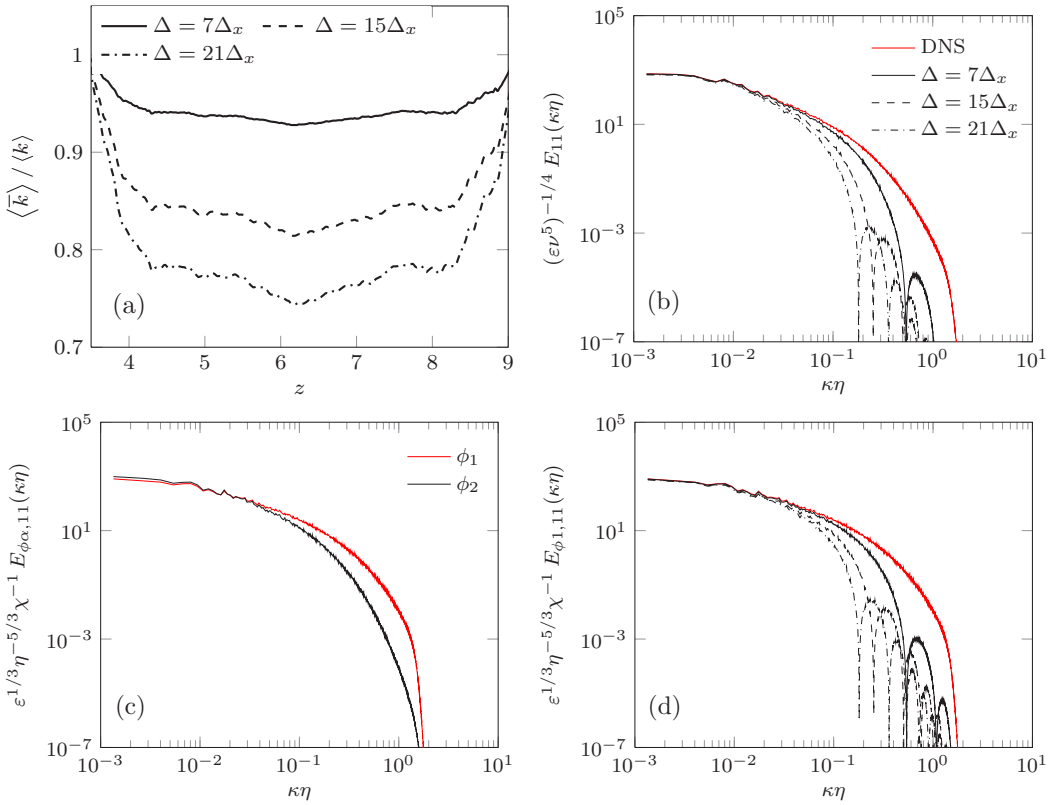

FIG. 3. (a) Ratio of the averaged filtered and unfiltered turbulent kinetic energy in the crosswise direction, (b) one-dimensional (1D) turbulence spectrum along the jet center, (c) 1D scalar spectrum of both passive scalars for the DNS, and (d) 1D scalar spectrum of ϕ_1. The spectra are normalized with the mean center-plane values of χ, η, and ε, respectively.

Due to the filtering procedure, the PDF of the scalar is slightly shifted towards smaller values, which also results in a continuous decrease of the chosen threshold value for the scalar. For a quantitative comparison of the interfaces detected in the simulation, PDFs of the difference between the TNTI position detected in the DNS and in the filtered data are shown in Figs. 6 and 7. Figure 6(a) shows the difference between the DNS interface and the interface detected in the filtered data when applying the vorticity criterion $\Delta_\omega = z_{I,\omega,\mathrm{DNS}} - z_{I,\omega,\mathrm{filtered}}$, whereas Fig. 6(b) shows these differences when the interface is detected with the scalar criterion applied to the unity-Schmidt-number scalar $\Delta_{\phi_1} = z_{I,\phi_1,\mathrm{DNS}} - z_{I,\phi_1,\mathrm{filtered}}$. While the PDF of the vorticity interface is nearly symmetric, the PDF of the scalar interface is more skewed, which is more pronounced with increasing filter width. Further, the corresponding statistical quantities are listed in Table II, where the mean values are standardized with the corresponding rms values σ_{Δ_ω} and $\sigma_{\Delta_{\phi_1}}$, respectively. Both PDFs broaden for larger filter widths. Smaller mean values are found for the vorticity interface, ranging from -0.0040 to 0.0315, while the mean values of the scalar interface range from 0.0154 to 0.0703. This indicates better statistical agreement of the original interface and the filtered interface for the vorticity criterion. It is also interesting to note that the vorticity interface obtains highest probabilities at differences to the original vorticity interface very close to zero (the maximum difference for $\Delta = 21\Delta_x$ is $\Delta_\omega/\sigma_{\Delta_\omega} = 0.1$), whereas the scalar interface obtains the highest probabilities at differences which are five times as large. Accordingly, the PDF of the difference between the position of the vorticity TNTI and the scalar TNTI is shown in Fig. 7. This PDF yields larger mean values and becomes

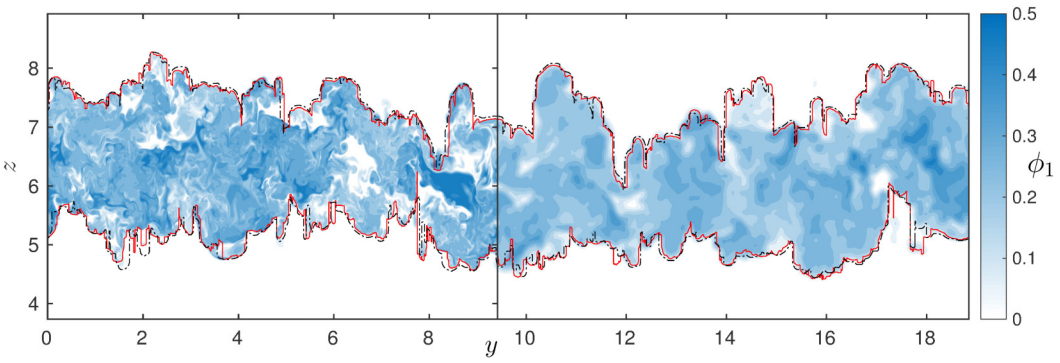

FIG. 4. Side-by-side comparison of the unfiltered left half and filtered right half ($\Delta = 21\Delta_x$) of the scalar distribution in a yOz plane. Additionally marked are the unfiltered TNTIs marked in red and the corresponding filtered TNTIs marked in black, both detected with the vorticity criterion.

broader with increasing filter width, indicating larger instantaneous differences between the vorticity and the scalar TNTI with increasing filter width. These increasing differences originate from the shift of the scalar TNTI with increasing filter width, while the vorticity TNTI remains closer to the original DNS interface as shown in Fig. 6. From these observations, it can be concluded that the vorticity criterion is more robust against filtering than the scalar criterion. For illustration, Fig. 8 shows the comparison between the TNTI of the original DNS data and of the four filtered interfaces marked on top of the original DNS data of the enstrophy and the unity-Schmidt-number scalar field. The interfaces detected with the vorticity criterion are shown in Fig. 8(a) and the interfaces detected with the scalar criterion are shown in Fig. 8(b). This comparison confirms the findings shown in Fig. 6. Although the vorticity criterion exhibits locally larger differences from the original DNS interface, also visible in larger rms values of Δ_ω (see Table II), the scalar interface exhibits a continuous offset to the original interface, particularly represented by larger mean values of Δ_{ϕ_1}.

The scalar interface width was additionally evaluated using the tangent at the steepest slope intersecting with 25% and 80% of the mean center-plane scalar value. A continuous increase of this interface width was found with increasing filter width. The interface width was evaluated as 0.03 for the original DNS data and 0.06, 0.10, and 0.14 for the corresponding filtered data with increasing filter width, respectively. The Taylor microscale was evaluated as $\lambda = \sqrt{10\frac{\nu}{\varepsilon}k} = 0.1$, where ε is the

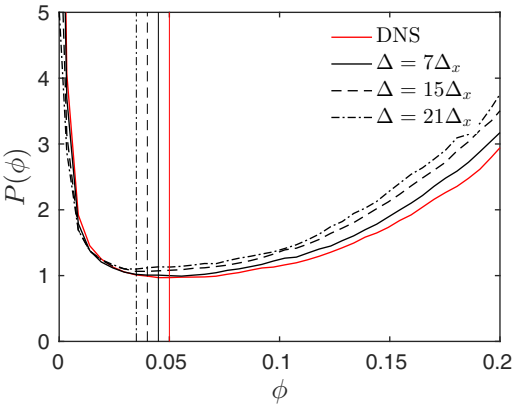

FIG. 5. The PDF of the unity-Schmidt-number scalar shown in the range $\phi_1 = [0,0.2]$.

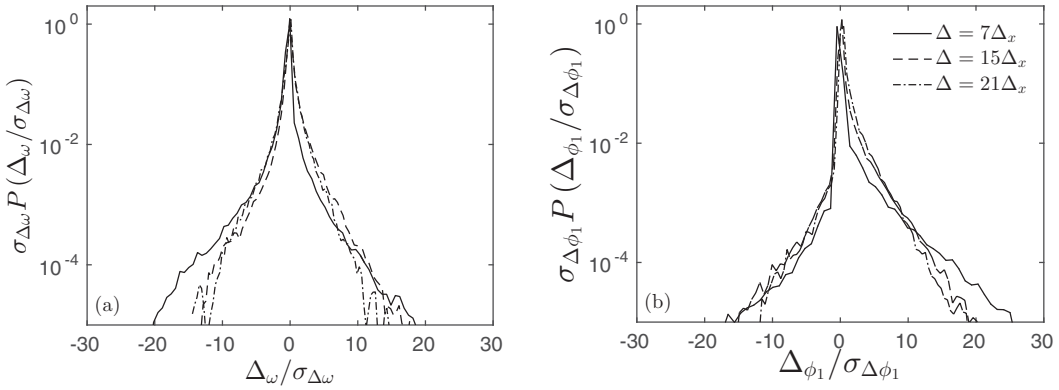

FIG. 6. The PDF of the differences between the DNS interface and the interface positions in the filtered data detected with (a) the vorticity criterion and (b) the scalar criterion for ϕ_1, respectively.

turbulent dissipation, showing that the scalar interface width is of the same order of magnitude as the Taylor microscale. A correlation of both quantities was suggested, e.g., by Gampert *et al.* [22].

The intermittency factor γ, introduced by Townsend [38] and shown, e.g., for a shear layer in [27], is almost constant for the different filtering procedures in comparison with the original DNS data (not shown). This is due to the large-scale wrinkling of the interface, which is retained by the filtering procedure. The variation from $\gamma = 0$ to $\gamma = 1$ proceeds over roughly 350 cells and is therefore less affected by the filtering procedure acting on 21 cells at maximum.

Consequently, the main characteristics of the turbulent-nonturbulent interface are maintained by the filtering procedure carried out in this work. The vorticity criterion is more robust against filtering and slightly larger discrepancies exist when using the scalar interface. These findings are in line with the work by Gampert *et al.* [28], who found good agreement in the PDF of the TNTI position provided the LES is highly resolved.

To analyze differential diffusion, the vorticity criterion for the interface detection is applied in the following to maintain independence from the two different scalar fields and to be consistent with the analyses in [26]. Further, the same TNTI is used for all filtering procedures in order to clearly identify the influence of filtering on differential diffusion and to avoid a superposition with differences that

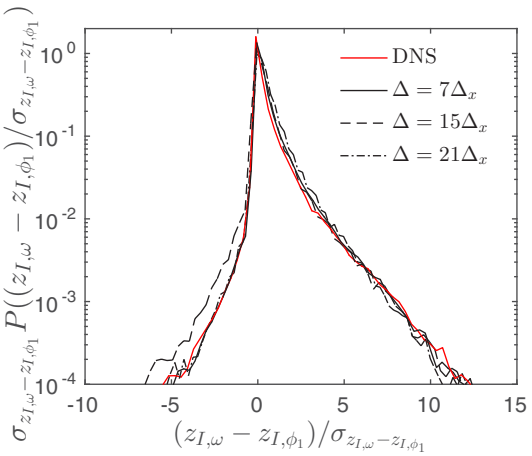

FIG. 7. The PDF of the differences between the interface positions detected with the vorticity criterion and the scalar criterion for ϕ_1, respectively. The mean values $z_{I,\omega} - z_{I,\phi_1}$ are 6.2, 9.7, 8.5 and 14.4, respectively.

TABLE II. Statistical quantities of the difference between the DNS interface and the interface positions in the filtered data detected with the vorticity criterion and the scalar criterion for ϕ_1, respectively.

	TNTI using ω			TNTI using ϕ_1		
Measure	$\Delta = 7\Delta_x$	$\Delta = 15\Delta_x$	$\Delta = 21\Delta_x$	$\Delta = 7\Delta_x$	$\Delta = 15\Delta_x$	$\Delta = 21\Delta_x$
mean	−0.0040	0.0315	0.0208	0.0154	0.0435	0.0703
rms	0.0737	0.1139	0.1474	0.0469	0.0804	0.0938

might occur due to the statistical differences of the interface position itself when detected on the filtered field.

B. Comparing differential diffusion between resolved and filtered data

Differential diffusion manifests itself as a deviation between the initially perfectly correlated turbulent scalar fields. Different measures to analyze and quantify differential diffusion can be used. In order to show the local deviation between the scalar fields, the joint PDF of the two scalars at the interface $P(\phi_1,\phi_2;z_I)$ is shown in Fig. 9 along with the conditional mean $\langle\phi_1|\phi_2;z_I\rangle$ comparing these distributions between the original and filtered data. With increasing filter width the joint PDF $P(\phi_1,\phi_2;z_I)$ becomes much narrower, corresponding to fewer excursions of large differences. Here $P(\phi_1,\phi_2;z_I)$ reveals a distinct maximum, which is increasing with increasing filter size, and fluctuations around the conditional mean become smaller. Also, the conditional mean approaches a straight line. These findings suggest that differential diffusion is locally less observable with increasing filter width.

Moreover, the differences between the two passive scalars $\Delta\phi = \phi_1 - \phi_2$ can be used for quantifying differential diffusion. The mean and rms of $\Delta\phi$ conditioned on the distance from the TNTI is shown in Fig. 10(a). It was shown in [26] that the conventional statistics give almost congruent mean scalar profiles, whereas significant differences were present in the conditional statistics. Figure 10(a) shows a large rms value of $\Delta\phi$ along the entire crosswise direction for the original DNS data. The filtering procedure significantly decreases the differences between the two scalars. This is especially visible in the peak of the mean profiles of $\Delta\phi$ since the value in the vicinity of the interface decreases by one order of magnitude. However, they all approach the same value in the turbulent core and converge already very near the interface. The rms decreases by a factor of 3 and consequently approaches a minimum of only 0.015. The rms profiles lose their peak at the TNTI leading to smooth curves from the irrotational outer flow to the turbulent jet core. Note that the presence of differential diffusion at large scales can first be seen in the rms values of scalar quantities (see, e.g., [8]). This also explains the moderate decrease of these values in comparison with their mean

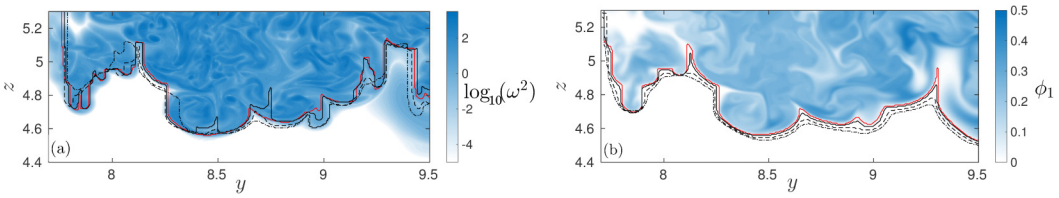

FIG. 8. Detail of the contour in a yOz plane comparing the interfaces of the original DNS data and the filtered data using (a) the vorticity criterion (logarithmical scale) marked on the enstrophy contour and (b) the scalar criterion for ϕ_1 marked on the unity-Schmidt-number scalar contour. The original DNS interface is marked in red and the interface detected on the filtered fields are marked in black with solid line, $\Delta = 7\Delta_x$; dashed line, $\Delta = 15\Delta_x$; and dash-dotted line, $\Delta = 21\Delta_x$.

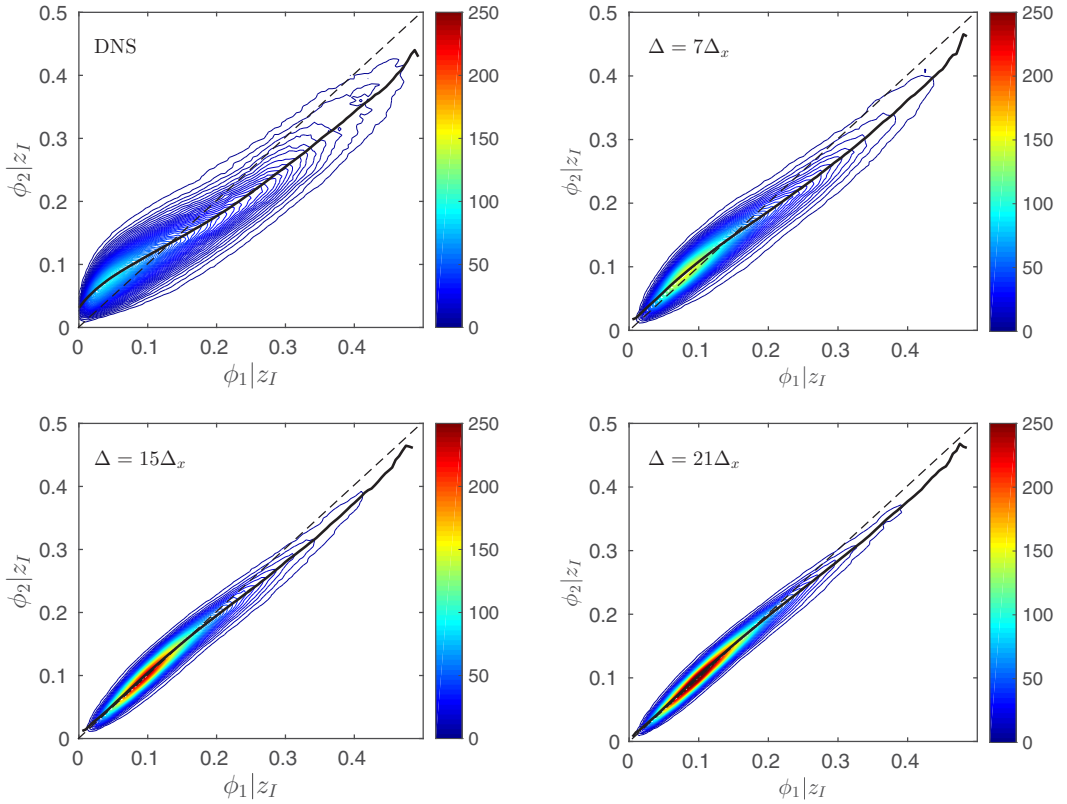

FIG. 9. Joint PDF $P(\phi_1,\phi_2;z_I)$ of the passive scalars and the conditional mean $\langle\phi_1|\phi_2;z_I\rangle$ (black solid line) at the TNTI. The bisecting line corresponding to no differential diffusion effects is also marked (black dashed line).

quantities leading to non-negligible values along the curve without distinct peaks at the TNTI, which shows that the importance of the TNTI on differential diffusion is not maintained in the filtered field. An additional quantification can be performed using the centered differential diffusion parameter as shown in [2]

$$Z = \frac{\phi_1}{\langle\phi_1\rangle} - \frac{\phi_2}{\langle\phi_2\rangle}, \tag{4}$$

where only the rms value is required to characterizes differential diffusion. This quantity is shown in Fig. 10(b). Again, a significant decrease of the maximum value in the vicinity of the TNTI but also in the plateau value of the turbulent core indicates a significant decrease of resolved differential diffusion.

It can be concluded that filtering with a large filter kernel in physical space leads to an overall decrease of differential diffusion in the mean profiles but also in the rms values. The filter kernel with a filter width $\Delta = 21\Delta_x$, which is a reasonable choice of filter size according to the resolved turbulent kinetic energy [see Fig. 3(a)], yields differential diffusion effects, which are one order of magnitude smaller than in the original unfiltered data. Further, differential diffusion is seen to be significantly underresolved near the TNTI, yet in the turbulent region it still persists, although also to a smaller degree.

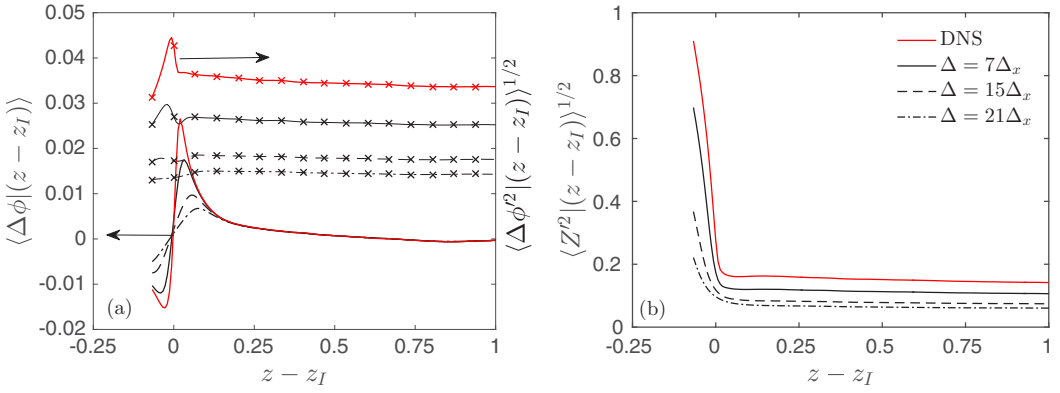

FIG. 10. (a) Comparison of the mean (lines) and rms (crosses) of the difference $\Delta\phi$ and (b) rms of the differential diffusion parameter Z conditioned on the distance from the TNTI between the unfiltered and filtered data.

C. Origin of differential diffusion at the TNTI

The physical mechanism behind differential diffusion is analyzed using the transport equation for the scalar difference $\Delta\phi$ as presented in [26], which reads

$$\underbrace{\frac{\partial \Delta\phi}{\partial t}}_{\text{local changes}} + \underbrace{u_i \frac{\partial \Delta\phi}{\partial x_i}}_{\text{convection}} = \underbrace{\frac{1}{\mathrm{Pe}_{0,1}} \frac{\partial^2 \Delta\phi}{\partial x_i \partial x_i}}_{\text{diffusion}} + \underbrace{\left(\frac{1}{\mathrm{Pe}_{0,1}} - \frac{1}{\mathrm{Pe}_{0,2}} \right) \frac{\partial^2 \phi_2}{\partial x_i \partial x_i}}_{\text{source term}}. \tag{5}$$

In order to evaluate the differences between the resolved and unresolved terms, the filtered transport terms are subtracted from the unfiltered transport terms, resulting in the subfilter terms as

$$\left(u_i \frac{\partial \Delta\phi}{\partial x_i} \right)' = u_i \frac{\partial \Delta\phi}{\partial x_i} - \overline{u_i \frac{\partial \Delta\phi}{\partial x_i}} \quad \text{(convection)}, \tag{6}$$

$$\left(\frac{\partial^2 \Delta\phi}{\partial x_i \partial x_i} \right)' = \frac{\partial^2 \Delta\phi}{\partial x_i \partial x_i} - \overline{\frac{\partial^2 \Delta\phi}{\partial x_i \partial x_i}} \quad \text{(diffusion)}, \tag{7}$$

$$\left(\frac{\partial^2 \phi_2}{\partial x_i \partial x_i} \right)' = \frac{\partial^2 \phi_2}{\partial x_i \partial x_i} - \overline{\frac{\partial^2 \phi_2}{\partial x_i \partial x_i}} \quad \text{(source term)}. \tag{8}$$

The single terms are then conditionally averaged over the distance from the TNTI and the resolved (shown in black) and unresolved terms (shown in blue) are presented in comparison with the original DNS terms in Fig. 11. First, all terms of the DNS data are significant at the TNTI, indicating the importance of this characteristic to the evolution and development of differential diffusion. The subfilter terms obtain a structure similar to the terms of the DNS data, whereas the filtered terms are comparatively small. The filtered terms decrease strongly at the TNTI but drop only moderately towards the turbulent core and this influences the structure of all three terms. Further, it is visible that the subfilter terms almost always exceed the resolved terms in the vicinity of the TNTI, except for the source term when filtered with the smallest filter width. For the convection and diffusion term, the subfilter terms almost approach the DNS terms for the medium and large filter width in the vicinity of the TNTI and correspondingly, the resolved terms approach zero, indicating that the large contribution of convection and diffusion at the TNTI is not recovered when using the filtered data. This is mainly caused by the significant decrease of $\Delta\phi$ itself with increasing filter width in contrast to ϕ_2, which defines the source term. The stronger decrease of $\Delta\phi$ is due to the fact that it is a quantity acting predominantly on the small scales. Thus, the source term exhibits better agreement between the filtered term and the original DNS term. Since the latter is the only term responsible

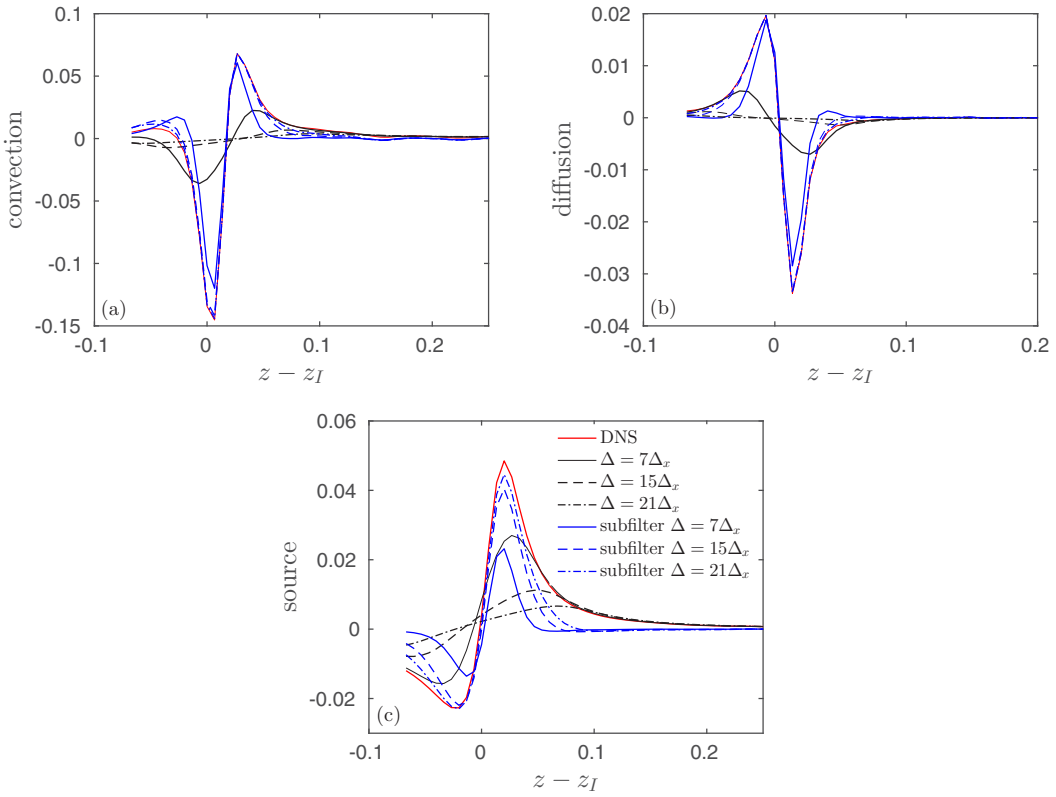

FIG. 11. Comparison of the (a) convection, (b) diffusion, and (c) source term of the transport equation for the difference $\Delta\phi$ conditioned on the distance from the TNTI between the DNS and the different filter widths.

for the generation of differential diffusion, it still originates near the TNTI of the resolved field but to a much lower extent. Consequently, a significant shift of origin and development of differential diffusion is observed when the transport equation for the scalar differences is evaluated using the filtered fields only. The large contribution of each term at the TNTI is not maintained in the filtered fields. The major part of all terms needs to be incorporated in subfilter models.

Filtering procedures strongly affect local gradients, which are particularly important for the development of differential diffusion. Thus, PDFs of the resolved and unresolved unity-Schmidt-number scalar gradient evaluated at the TNTI are shown in Fig. 12(a). Accordingly, the difference between the diffusive fluxes $|\mathbf{j}_1 - \mathbf{j}_2|$ can be evaluated, where

$$\mathbf{j}_\alpha = -\frac{1}{\mathrm{Pe}_{0,\alpha}} \nabla \phi_\alpha. \tag{9}$$

A comparison of $|\mathbf{j}_1 - \mathbf{j}_2|$ between the mean resolved and unresolved quantities conditioned on the distance from the TNTI position is shown in Fig. 12(b). The PDF of the scalar gradient of the original DNS data evaluated at the TNTI exhibits a flat distribution over a large range of scalar gradients. Filtering leads to a separation in predominantly small gradients in the resolved field and predominantly large gradients in the subfilter field. With increasing filter width the PDF of the resolved scalar gradient becomes narrower, leading to smaller mean scalar gradients. Simultaneously, the corresponding subfilter PDFs become broader. This shows that large local gradients move to subfilter scale. This behavior is particularly important in the vicinity of the TNTI since here the largest local gradients occur in a statistical sense. This also involves the decrease of the resolved diffusion term in the scalar transport equation, which was also found to be dominant in the vicinity

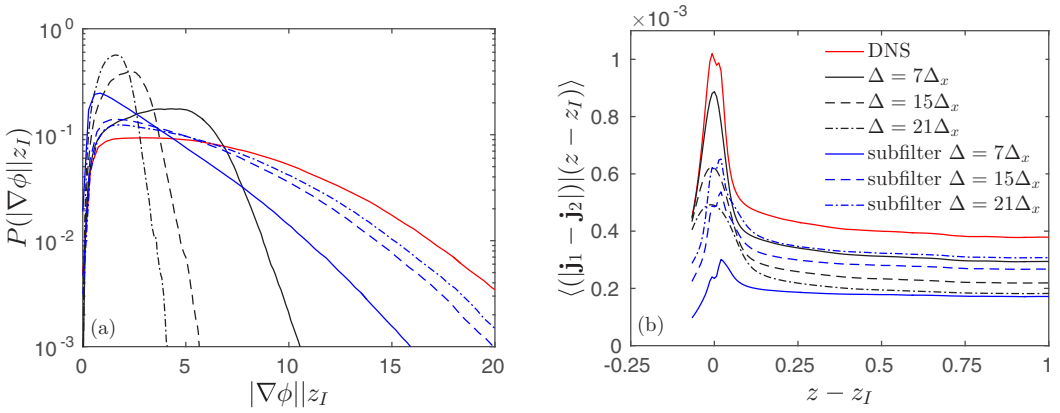

FIG. 12. (a) Comparison of the PDF of the resolved and unresolved magnitude of the scalar gradient evaluated at the TNTI and (b) mean profiles of the difference between the diffusive fluxes conditioned on the distance from the TNTI between the unfiltered and filtered data.

of the interface (see [39]). Consequently, it becomes necessary to include them in subfilter models. Maragkos *et al.* [10] performed a numerical analysis of differential diffusion in a nonreactive jet simulation using LESs. Significant differential diffusion effects were detected and a decrease of these effects with increasing Reynolds number was confirmed. It is important to underline that the resolution of the LES they performed was very high and resolved scales started in the dissipation range. Hence, their LES is rather comparable to the filter width $\Delta = 7\Delta_x$ in this analysis. According to the results above, Fig. 12(b) shows the differences between the diffusive fluxes comparing the different filter widths. Large differences exist near the TNTI for all filter widths and they decrease dramatically towards the turbulent core. For the smallest filter width, the major part of this difference is resolved. However, when increasing the filter width further, the difference of the diffusive flux in the resolved and unresolved fields is of the same order of magnitude in the vicinity of the TNTI and the unresolved term even exceeds the resolved term in the turbulent core, which clearly shows that filtering has different effects in the vicinity of the TNTI and the turbulent core.

In order to take apart the diffusive flux difference and to illustrate the mechanism responsible for the departure between the two scalars, the scalar gradient alignment using the mean of the cosine of the angle between the scalar gradients

$$\langle \cos\varphi|(z - z_I)\rangle = \left\langle \frac{\nabla\phi_1 \cdot \nabla\phi_2}{|\nabla\phi_1||\nabla\phi_2|}\middle|(z - z_I)\right\rangle \tag{10}$$

and the mean ratio of the magnitude of the diffusive fluxes $\mathbf{j}_\alpha$,

$$\langle R|(z - z_I)\rangle = \left\langle \frac{|\mathbf{j}_1|}{|\mathbf{j}_2|}\middle|(z - z_I)\right\rangle = \left\langle \frac{\mathrm{Pe}_{0,2}|\nabla\phi_1|}{\mathrm{Pe}_{0,1}|\nabla\phi_2|}\middle|(z - z_I)\right\rangle, \tag{11}$$

is shown in Fig. 13. In [26] it was concluded that a strong alignment with simultaneous differences in the magnitude of the diffusive fluxes causes differential diffusion, which is very pronounced in the vicinity of the TNTI. When a filtering procedure is applied, the alignment shows a global increase and becomes more and more similar near the TNTI and the turbulent core. This overall increase of alignment is caused by the reduction of the large local gradients due to filtering the large wave numbers that particularly contain the scalar differences. The ratio of the diffusive fluxes decreases with increasing filter width. Consequently, the expansion of the alignment towards the turbulent core and the decrease of the diffusive flux ratio lead to a significant change in the development of differential diffusion with increasing filter width. The significance of differential diffusion at the TNTI is not captured and due to the overall decrease of local gradients, the origin of differential diffusion

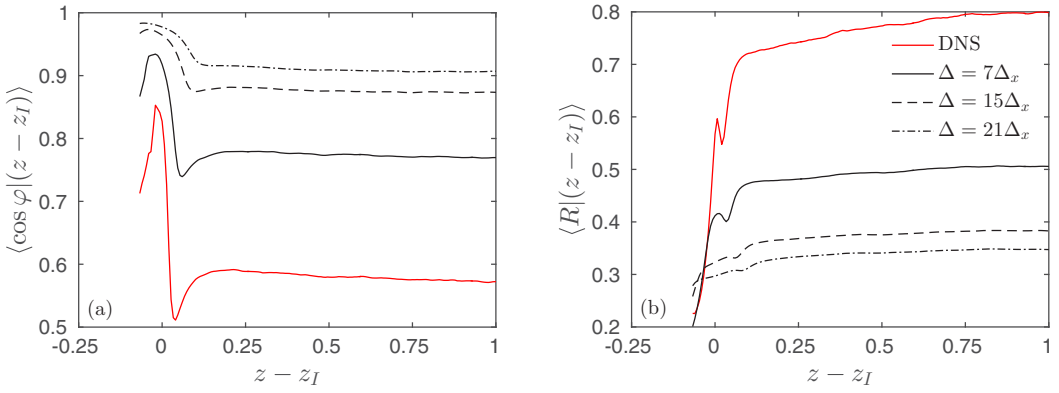

FIG. 13. (a) Comparison of the conditional mean cosine of the angle between the scalars and (b) the ratio of their diffusive fluxes conditioned on the distance from the TNTI between the DNS and filtered data.

would dramatically decrease, which must instead be included in appropriate subfilter modeling approaches.

IV. CONCLUSION

The existence of differential diffusion and the impact of the TNTI on the mechanisms responsible for it were compared between resolved and subfilter scales in explicitly filtered DNS data of a temporally evolving turbulent plane jet transporting two passive scalars with Schmidt numbers of unity and 0.25 [26]. The investigation was twofold. The statistics of the TNTI using the filtered fields were investigated first and then differential diffusion was statistically analyzed. The results can be summarized as follows.

(i) The comparison of the TNTI position between the original DNS data and the filtered data shows that the statistics of the TNTI are maintained by filtering the field. The vorticity-based TNTI is more robust against filtering than the scalar-based TNTI.

(ii) Differential diffusion significantly decreases with increasing filter width, even in the rms values of the differential diffusion parameter. The dominance of differential diffusion at the TNTI is preserved but decreases significantly.

(iii) The transport equation for the scalar difference shows that the major contribution of all terms at the TNTI is not maintained. Different effects of filtering on the three terms of the transport equation lead to differences in evolution and development of differential diffusion, necessitating the use of subfilter models.

(iv) Filtering significantly reduces the local gradients, which are the driving force for differential diffusion. This is particularly important in the vicinity of the TNTI since here the largest local gradients occur in a statistical sense. Consequently, differences between the diffusive fluxes become more pronounced at subfilter scale, but to a different extent at the TNTI and in the turbulent jet core.

(v) Due to the decrease of the local gradients, resolved scalar gradients are globally better aligned, while the ratio of the diffusive fluxes decreases with filtering. This would result in an overall change of origin and development of differential diffusion, suggesting that the large contribution to differential diffusion at the TNTI needs an appropriate subfilter model.

ACKNOWLEDGMENTS

The authors gratefully acknowledge the computing time provided by the Gauss Center for Supercomputing/Leibniz Supercomputing Center (Grant No. pr74li) and the computing time granted

on the supercomputer JUQUEEN at Forschungszentrum Jülich [40] by the John von Neumann Institute for Computing.

[1] R. W. Bilger, Reaction rates in diffusion flames, Combust. Flame **30**, 277 (1977).
[2] T. M. Lavertu, L. Mydlarski, and S. J. Gaskin, Differential diffusion of high-Schmidt-number passive scalars in a turbulent jet, J. Fluid Mech. **612**, 439 (2008).
[3] L. L. Smith, R. W. Dibble, L. Talbot, R. S. Barlow, and C. D. Carter, Laser Raman scattering measurements of differential molecular diffusion in nonreacting turbulent jets of H_2/CO_2 mixing with air, Phys. Fluids **7**, 1455 (1995).
[4] R. W. Dibble and M. B. Long, Investigation of differential diffusion in turbulent jet flows using planar laser Rayleigh scattering, Combust. Flame **143**, 644 (2005).
[5] C. J. Brownell and L. K. Su, Planar laser imaging of differential molecular diffusion in gas-phase turbulent jets, Phys. Fluids **20**, 035109 (2008).
[6] V. Nilsen and G. Kosály, Differentially diffusing scalars in turbulence, Phys. Fluids **9**, 3386 (1997).
[7] P. K. Yeung, M. C. Sykes, and P. Vedula, Direct numerical simulation of differential diffusion with Schmidt numbers up to 4.0, Phys. Fluids **12**, 1601 (2000).
[8] M. Ulitsky, T. Vaithianathan, and L. R. Collins, A spectral study of differential diffusion of passive scalars in isotropic turbulence, J. Fluid Mech. **460**, 1 (2002).
[9] Y.-H. Dong, X.-Y. Lu, and L.-X. Zhuang, Large eddy simulation of turbulent channel flow with mass transfer at high-Schmidt numbers, Int. J. Heat Mass Transfer **46**, 1529 (2003).
[10] G. Maragkos, P. Rauwoens, D. Fauconnier, and B. Merci, Large eddy simulations of differential molecular diffusion in non-reacting turbulent jets of H_2/CO_2 mixing with air, Phys. Fluids **26**, 025102 (2014).
[11] V. Bergmann, W. Meier, D. Wolff, and W. Stricker, Application of spontaneous Raman and Rayleigh scattering and 2D LIF for the characterization of a turbulent $CH_4/H_2/N_2$ jet diffusion flame, Appl. Phys. B **66**, 489 (1998).
[12] A. Sevault, M. Dunn, R. S. Barlow, and M. Ditaranto, On the structure of the near field of oxy-fuel jet flames using Raman/Rayleigh laser diagnostics, Combust. Flame **159**, 3342 (2012).
[13] R. S. Barlow, M. J. Dunn, and G. Magnotti, Preferential transport effects in premixed bluff-body stabilized CH_4/H_2 flames, Combust. Flame **162**, 727 (2015).
[14] E. R. Hawkes, R. Sankaran, J. C. Sutherland, and J. H. Chen, Scalar mixing in direct numerical simulations of temporally evolving plane jet flames with skeletal CO/H_2 kinetics, Proc. Combust. Inst. **31**, 1633 (2007).
[15] K. K. J. Rang Dinesh, X. Jiang, J. A. van Oijen, R. J. N. Bastiaans, and L. P. H. de Goey, Hydrogen-enriched nonpremixed jet flames: Effects of preferential diffusion, Int. J. Hydrogen Energy **38**, 4848 (2013).
[16] C. Bruno, V. Sankaran, H. Kolla, and J. H. Chen, Impact of multi-component diffusion in turbulent combustion using direct numerical simulations, Combust. Flame **162**, 4313 (2015).
[17] H. Pitsch, Unsteady flamelet modeling of differential diffusion in turbulent jet diffusion flames, Combust. Flame **123**, 358 (2000).
[18] S. Nambully, P. Domingo, V. Moureau, and L. Vervisch, in *Proceedings of the Seventh International Symposium on Turbulence, Heat and Mass Transfer, Palermo, 2012* (International Centre for Heat and Mass Transfer, Danbury, 2012).
[19] W. Han, V. Raman, and Z. Chen, LES/PDF modeling of autoignition in a lifted turbulent flame: Analysis of flame sensitivity to differential diffusion and scalar mixing time-scale, Combust. Flame **171**, 69 (2016).
[20] C. B. da Silva, J. C. R. Hunt, I. Eames, and J. Westerweel, Interfacial layers between regions of different turbulence intensity, Annu. Rev. Fluid Mech. **46**, 567 (2014).
[21] T. Watanabe, T. Naito, Y. Sakai, K. Nagata, and Y. Ito, Mixing and chemical reaction at high Schmidt number near turbulent/nonturbulent interface in planar liquid jet, Phys. Fluids **27**, 035114 (2015).

[22] M. Gampert, V. Narayanaswamy, P. Schaefer, and N. Peters, Conditional statistics of the turbulent/non-turbulent interface in a jet flow, J. Fluid Mech. **731**, 615 (2013).
[23] J. Westerweel, C. Fukushima, J. M. Pedersen, and J. C. R. Hunt, Momentum and scalar transport at the turbulent/non-turbulent interface of a jet, J. Fluid Mech. **631**, 199 (2009).
[24] M. Holzner, B. Lüthi, A. Tsinober, and W. Kinzelbach, Acceleration, pressure and related quantities in the proximity of the turbulent/non-turbulent interface, J. Fluid Mech. **639**, 153 (2009).
[25] C. B. da Silva and J. C. F. Pereira, Invariants of the velocity-gradient, rate-of-strain, and rate-of-rotation tensors across the turbulent/nonturbulent interface in jets, Phys. Fluids **20**, 055101 (2008).
[26] F. Hunger, M. Gauding, and C. Hasse, On the impact of the turbulent/non-turbulent interface on differential diffusion in a turbulent jet flow, J. Fluid Mech. **802**, R5 (2016).
[27] M. Gampert, J. Boschung, F. Hennig, M. Gauding, and N. Peters, The vorticity versus the scalar criterion for the detection of the turbulent/non-turbulent interface, J. Fluid Mech. **750**, 578 (2014).
[28] M. Gampert, K. Kleinheinz, N. Peters, and H. Pitsch, Experimental and numerical study of the scalar turbulent/non-turbulent interface layer in a jet flow, Flow Turbul. Combust. **92**, 429 (2014).
[29] S. K. Lele, Compact finite difference schemes with spectral-like resolution, J. Comput. Phys. **103**, 16 (1992).
[30] A. W. Cook, W. Cabot, and P. L. Miller, The mixing transition in Rayleigh-Taylor instability, J. Fluid Mech. **511**, 333 (2004).
[31] M. Roger, C. B. da Silva, and P. J. Coelho, Analysis of the turbulence-radiation interactions for large eddy simulations of turbulent flows, Int. J. Heat Mass Transfer **52**, 2243 (2009).
[32] G. Balarac, A. G. Kosovichev, O. Brugière, A. A. Wray, and N. N. Mansour, Studying Turbulence Using Numerical Simulation Databases—XIII, in *Center for Turbulence Research, Proceedings of the 2010 Summer Program* (Stanford University Press, Stanford, 2010), p. 503.
[33] A. J. Fager, J. Liu, and S. C. Garrick, Hybrid simulations of metal particle nucleation: *A priori* and *a posteriori* analyses of the effects of unresolved scalar interactions on nanoparticle nucleation, Phys. Fluids **24**, 075110 (2012).
[34] A. Donini, R. J. M. Bastiaans, J. A. van Oijen, M. S. Day, and L. P. H. de Goey, An a priori DNS subgrid analysis of the presumed β-PDF model, Int. J. Hydrogen Energy **40**, 12811 (2015).
[35] S. B. Pope, *Turbulent Flows* (Cambridge University Press, Cambridge, 2010).
[36] D. K. Bisset, J. C. R. Hunt, and M. M. Rogers, The turbulent/non-turbulent interface bounding a far wake, J. Fluid Mech. **451**, 383 (2002).
[37] R. R. Prasad and K. R. Sreenivasan, Scalar interfaces in digital images of turbulent flows, Exp. Fluids **7**, 259 (1989).
[38] A. A. Townsend, Local isotropy in the turbulent wake of a cylinder, Aust. J. Chem. **1**, 161 (1948).
[39] T. Watanabe, Y. Sakai, K. Nagata, Y. Ito, and T. Hayase, Turbulent mixing of passive scalar near turbulent and non-turbulent interface in mixing layers, Phys. Fluids **27**, 085109 (2015).
[40] M. Stephan and J. Docter, JUQUEEN: IBM Blue Gene/Q® Supercomputer System at the Jülich Supercomputing Centre, J. Large-Scale Res. Fac. JLSRF **1**, 1 (2015).